OPEN ACCESS



A Giant Shell of Ionized Gas Discovered near M82 with the Dragonfly Spectral Line Mapper Pathfinder

Abstract

We present the discovery of a giant cloud of ionized gas in the field of the starbursting galaxy M82. Emission from the cloud is seen in H\$\alpha\$ and [N II] \$\lambda 6583\$ in data obtained though a small pathfinder instrument used to test the key ideas that will be implemented in the Dragonfly Spectral Line Mapper, an upcoming ultranarrow-bandpass imaging version of the Dragonfly Telephoto Array. The discovered cloud has a shell-like morphology with a linear extent of 0°.8 and is positioned 0°.6 northwest of M82. At the heliocentric distance of the M81 group, the cloud's longest angular extent corresponds to 55 kpc and its projected distance from the nucleus of M82 is 40 kpc. The cloud has an average H\$\alpha\$ surface brightness of 2 × 10^{-18} erg cm^{-2} s^{-1} arcsec^{-2}. The [N II] \$\lambda 6583/H\$\alpha\$ line ratio varies from [N II]/H\$\alpha\$ \$\sim 0.2\$ to [N II]/H\$\alpha\$ \$\sim 1.0\$ across the cloud, with higher values found in its eastern end. Follow-up spectra obtained with Keck LRIS confirm the existence of the cloud and yield line ratios of [N II] \$\lambda 6583/H\$\alpha\$ = 0.340 \pm 0.003\$ and [S II] \$\lambda 6731/H\$\alpha\$ = 0.64 \pm 0.03\$ in the cloud. This giant cloud of material could be lifted from M82 by tidal interactions or by its powerful starburst. Alternatively, it may be gas infalling from the cosmic web, potentially precipitated by the superwinds of M82. Deeper data are needed to test these ideas further. The upcoming Dragonfly Spectral Line Mapper will have 120 lenses, 40× more than in the pathfinder instrument used to obtain the data presented here.

Unified Astronomy Thesaurus concepts: Circumgalactic medium (1879); Galaxy evolution (594); Intergalactic medium (813); Intergalactic gas (812); Intergalactic clouds (809)

1. Introduction

The M81 (NGC 3031) group of galaxies is one of the richest associations of galaxies in the local universe. The system has been well studied at many wavelengths, all the way from the gamma-ray regime through to the radio. The group contains the nearest ongoing major merger, at 3.66 Mpc (Tully et al. 2013), with H I observations showing significant neutral gas throughout the field, including clear tidal disruptions and interactions between M81, M82 (NGC 3034), and NGC 3077, the three most prominent galaxies in the group (Yun et al. 1994; Chynoweth et al. 2008; de Blok et al. 2018; Sorgho et al. 2019). Within the complicated debris field of the merger seen at all scales, the individual galaxies are also rich in structure: M81 is a face-on grand design spiral galaxy with a plethora of H II regions (Stanghellini et al. 2014) and star formation extending far past the disk (de Mello et al. 2008; Okamoto et al. 2015;

Original content from this work may be used under the terms of the Creative Commons Attribution 4.0 licence. Any further distribution of this work must maintain attribution to the author(s) and the title of the work, journal citation and DOI.

Harmsen et al. 2017), while M82 is the nearest starburst galaxy, with large-scale high-velocity asymmetrical outflows (Shopbell & Bland-Hawthorn 1998).

The M81 group is a prime target for mapping diffuse $H\alpha$ emission on large scales to search for evidence of circumgalactic gas fueling the star formation in the galaxies. Ionized gas visible through $H\alpha$ emission is predicted to reside in the circumgalactic medium and halos of galaxies in the local universe (Lokhorst et al. 2019), but is extremely difficult to observe (e.g., requiring stacking of millions of sightlines through galaxies to detect; Zhang et al. 2018a). The large-scale H I emission encompassing the group (Yun et al. 1994; Chynoweth et al. 2008; de Blok et al. 2018; Sorgho et al. 2019) and the well-known " $H\alpha$ cap" at a projected 11 kpc distance from the nucleus of M82 (Devine & Bally 1999; Lehnert et al. 1999) make this group the ideal target for searching for extended ionized emission, which should exist on scales similar to that of the H I emission at very faint levels.

In this paper we present the deepest wide field-of-view imaging of $H\alpha$ and [N II] emission from the M81 group published to date. These observations were carried out with an upgraded version of the Dragonfly Telephoto Array (Dragonfly; Abraham & van Dokkum 2014) equipped with instrumentation

¹² NASA Hubble Fellow.

to enable ultranarrow-bandpass imaging capability (see Lokhorst et al. 2020, for details). The large field of view and $\approx 3''$ resolution of the Dragonfly array, combined with its excellent control of systematics and light scattering, make it well suited to imaging extremely low-surface-brightness, extended structures, such as ultradiffuse galaxies, galactic outskirts, and tidal features (e.g., Merritt et al. 2014; van Dokkum et al. 2015; Zhang et al. 2018b; Gilhuly et al. 2020). The addition of ultranarrowband filters enables the detection of low-surface-brightness line emission from diffuse gas outside the galactic disk (Lokhorst et al. 2019; Bland-Hawthorn et al. 2017). In this paper we outline the telescope, observing processes, and data reduction procedure for an imaging campaign carried out on the M81 group of galaxies in the spring of 2020. We present the resulting $H\alpha$ and [NII] images, and report the discovery of a giant intragroup shell of ionized gas (with a linear extent of 0.8° or \approx 55 kpc at the distance of the M81 group). Potential origins of the shell are discussed along with our current knowledge of the M81 group.

2. Observations

2.1. Primary DSLM Observations

Narrowband imaging of $H\alpha$ and [N II] emission from the M81 group of galaxies was collected with a pathfinder version of the Dragonfly Spectral Line Mapper (DSLM) located in Mayhill, New Mexico, at New Mexico Skies Observatories. The pathfinder DSLM is a three-lens version of the Dragonfly Telephoto Array with Dragonfly Filter-Tilter instrumentation that implements ultranarrow-bandpass imaging capability on the telescope as described in Lokhorst et al. (2020). The pathfinder DSLM consists of two Canon 400 mm f/2.8 L IS II USM telephoto lenses and one Canon 400 mm f/2.8 L IS III USM telephoto lens, each with a 14.3 cm diameter aperture. Attached to each lens is an SBIG Aluma 694 camera with a Sony ICX-694ALG CCD sensor, which has an angular scale of 2.45" per pixel, resulting in a $1^{\circ}4 \times 1^{\circ}9$ field of view. Mounted on the front of each lens is a Dragonfly Filter-Tilter that holds a 152 mm diameter filter. The filters used for these observations have a central wavelength of 659.9 nm and FWHM of 3.1 nm. The Filter-Tilters have an allowed filter rotation range of -20° to $+20^{\circ}$ around an axis perpendicular to the optical axis, which enables the central wavelength to be shifted blueward from its intrinsic value by up to 8 nm. In addition to the Filter-Tilter instrumentation, the Dragonfly pathfinder is equipped with electroluminescent flat field panels that are used to collect flat-field images after each science exposure, allowing precise illumination corrections to be obtained at each filter tilt and pointing.

Observations were carried out from 2020 February to 2020 May. The observations followed the Dragonfly automated observing model, where the telescope is set up every night for observing at the beginning of the night and the telescope carries out observations autonomously, adapting to changing weather conditions and pausing observations when necessary. In total, this resulted in 73 nights of data collection over the months of 2020 February to June and a total of 652 on-target science frames collected with individual exposure times of 1800 s. The data were taken with the filters at two different tilts: 12.5° to target the H α λ 6563 emission line and 7° to target the [N II] λ 6583 emission line. Tilting the filters smoothly shifts the filter central wavelength, and these two tilts shifted the filter central wavelengths to 656.3 nm and 683.5 nm, respectively.

The final science images (after removing "bad" frames; see the Appendix for details) consisted of a total of 31.7 hr of integration on the H α line and 15.3 hr on the [N II] line with the three-lens pathfinder DSLM. The field of view of the final science images is $\sim\!2^\circ\times3^\circ$ after dithering (which was carried out in an eight-point 15′ pattern) and including the $\sim\!30'$ offsets of the lens pointings.

To verify the existence of some of the features reported here, additional $H\alpha$ data were obtained in the spring of 2021 with the pathfinder DSLM on a field located northwest of M82 (targeting a region of bright $H\alpha$ emission). The final science image in this pointing consisted of 8.3 hr of integration with the three-lens pathfinder DSLM, and was reduced using data processing techniques identical to those used to reduce the initial set of observations, as described below.

Observations of the M81 group were also carried out with the original Dragonfly Telephoto Array (as described in, e.g., Danieli et al. 2020) equipped with broadband g and r Sloan Digital Sky Survey filters. These data were used to subtract the stellar continuum and Galactic cirrus emission from the $H\alpha$ and [N II] data. Broadband observations of the M81 group were carried out on 2020 May 16, gathering a total of 12.5 minutes of integration time on-target in the r band and 10 minutes in the g band. Similar imaging was obtained in spring 2021 for the M82 field pointing. The continuum Dragonfly image is shown in the top left panel of Figure 1, with the bright inner regions of M81 and M82 replaced by color composite images from the Digital Sky Survey. The top right panel of Figure 1 shows an HI emission map of the M81 group of galaxies from de Blok et al. (2018) over the same field of view. The bottom row of Figure 1 contains insets with a smaller field of view from the Dragonfly r-band image, the pathfinder DSLM H α image, and the pathfinder DSLM [N II] image.

2.2. DSLM Data Reduction

The Dragonfly data were reduced using a modified version of DFReduce (see Danieli et al. 2020 for a description of the Dragonfly data reduction pipeline). We outline the steps of the pipeline and summarize differing procedures for the narrowband data reduction in the Appendix. Continuum light was removed from the final science frames by subtracting a scaled r-band image from the narrowband frames. The scaling factor was determined by iteration; as the scaling factor was varied, the M82 galactic disk was monitored to ensure that the continuum emission was subtracted completely while not oversubtracting parts of the disk. To determine the error introduced by the continuum subtraction, the emission line flux was calculated (using the flux calibration described below) for two scaling factors that resulted in over- and undersubtracting the M82 disk, respectively $(r/H\alpha = 11.3 \text{ and } r/H\alpha = 12.3).$ The resulting fractional error in regions of interest was found to be less than 1%. This low error is due to the fact that the regions of interest have limited overlap with galactic stellar light and Galactic cirrus emission so the noise introduced from continuum sources is minimal. The continuum-subtracted ${
m H}lpha$ data are displayed in Figure 2. The left panel shows the M81 group image while the right shows the M82 field image.

The images collected by the pathfinder DSLM are of such wide field of view that they contain both the M82 and M81 galaxies as well as other members of the M81 group. We used the H II regions in M81 to carry out a flux calibration of the images by measuring the emission line fluxes of H II regions and

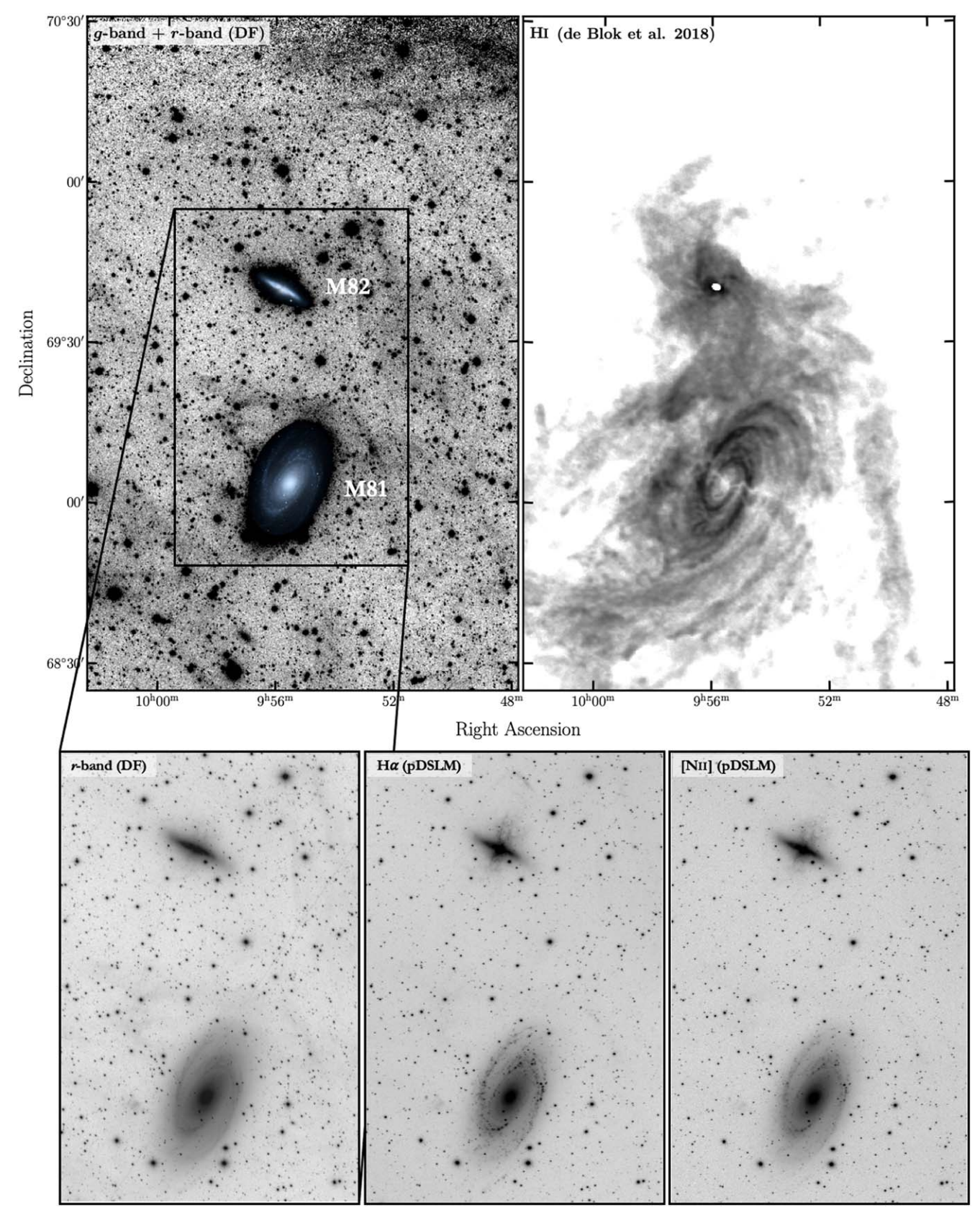


Figure 1. The top left panel displays the Dragonfly Telephoto Array g- and r-band combined image of M81 and M82 with bright inner galactic regions replaced by continuum-band images from the Digital Sky Survey for reference. This field contains a large amount of galactic cirrus, e.g., the northwest (top right) corner of this field with particularly bright cirrus. The H I emission map from de Blok et al. (2018) over the same field of view and log-scaled is displayed for comparison in the top right panel. The bottom row displays insets of the above field of view in the r band (Dragonfly), H α (pathfinder DSLM), and [N II] (pathfinder DSLM); these images are log-scaled to showcase both the bright inner galactic regions and faint diffuse extragalactic emission.

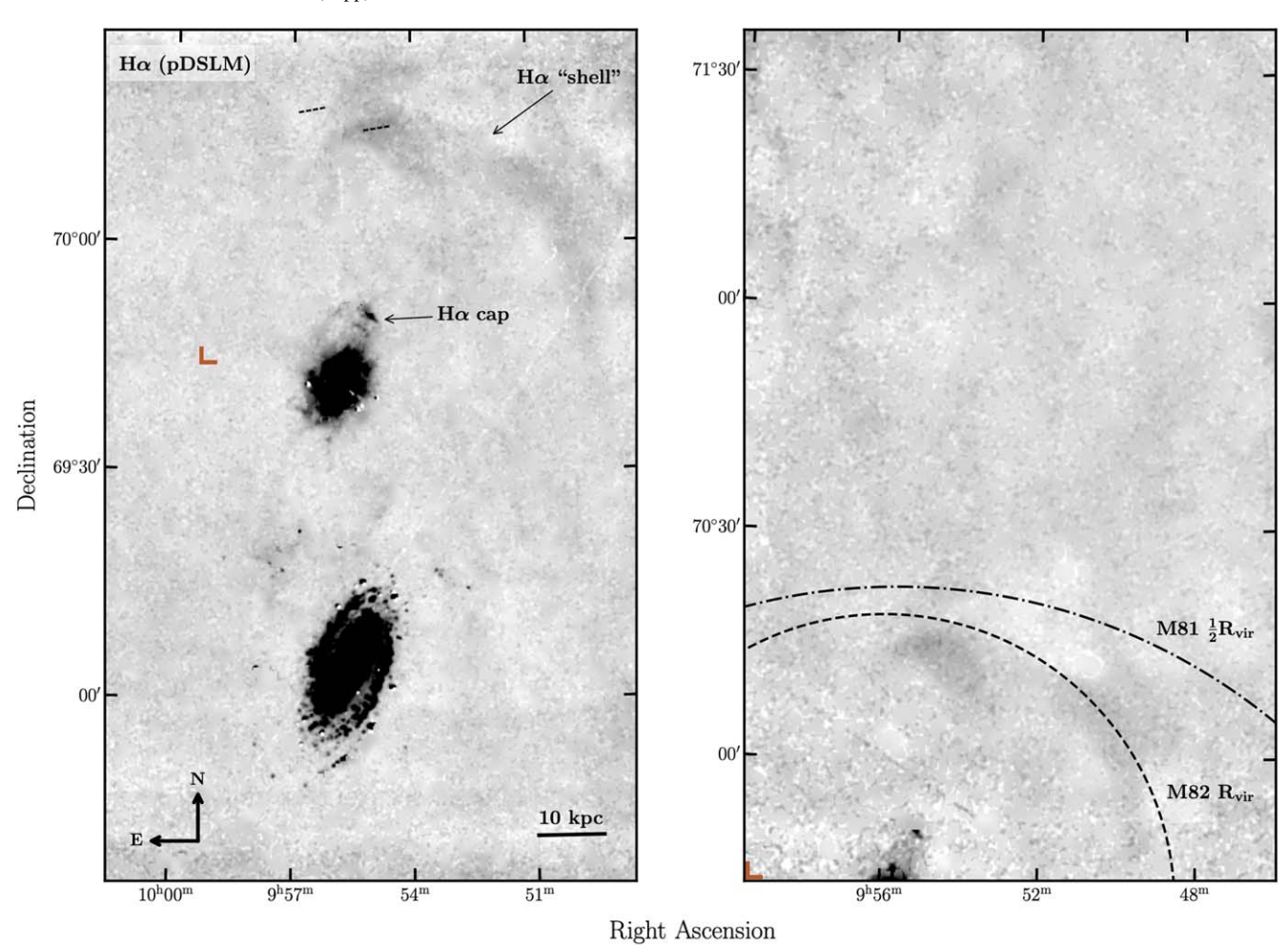


Figure 2. The pathfinder DSLM $H\alpha$ map of the galaxies M81 and M82, continuum-subtracted, smoothed with a Gaussian filter of 1.5 pixels FWHM, and masked. Masked regions are replaced with the median of nearby unmasked pixels. The $H\alpha$ "shell" is a region of bright emission in the outer halo of M82. The $H\alpha$ cap is a previously discovered ionized gas cloud in the circumgalactic medium of M82 (Devine & Bally 1999; Lehnert et al. 1999). The dashed lines indicate the slit locations used in the Keck LRIS follow-up observations to the $H\alpha$ shell (both off-target and on-target slits are shown). The bands of darker/lighter emission across the bottom and top of the $H\alpha$ image are regions that are only in a subset of the frames due to the dither pattern and have lower signal-to-noise ratio. A pathfinder DSLM $H\alpha$ map of a field located to the northeast of M82 is shown on the right (with the same smoothing and masking as the image on the left). Note that this image has four times less exposure time than the left image, with correspondingly lower signal-to-noise ratio. There are no extensions to the shell of the same signal-to-noise ratio as the shell in this image, which suggests that the shell is a condensed structure and not part of a larger Galactic stream of gas. The virial radius of M82 (\approx 44 kpc) is indicated by the dashed black circle. The half-virial radius of M81 is indicated for comparison (dashed-dotted line), where it is assumed that the galaxies are at the same radial heliocentric distance. The red corner mark in both images indicates the southeast origin of the M82 field image for reference.

comparing them to values in the published literature on the M81 H II regions. Linear fits between the flux measurements from the pathfinder DSLM data and published flux values from Lin et al. (2003) and Patterson et al. (2012) are shown in Figure 3. The two sources of published flux values are in good agreement with one another. The resulting fit using both published data sets is $\log_{10}(F \text{ [erg s}^{-1} \text{ cm}^{-2}]) = a \log_{10}(F \text{ [counts]}) + b$ where $a = 1.00 \pm 0.01$ and $b = -0.86 \pm 0.04$. Comparing the fits between the two data sets results in a maximum error of 9% for the flux calibration. With this calibration, the surface brightness limit of the H α data is found to be $\approx 5 \times 10^{-19} \text{ erg cm}^{-2} \text{ s}^{-1} \text{ arcsec}^{-2}$ or roughly 0.1 Rayleigh at the 3σ level on a spatial scale of 4′.

2.3. Supplementary Keck LRIS Observations

Observations with the Keck Observatory Low Resolution Imaging Spectrograph (LRIS) with a 1.5" longslit were also collected to verify the existence of observed features in the narrowband data (a total of 1200 s on-target and 1200 s off-target on both the red and blue sides were collected; the slit locations are

shown in the left panel of Figure 2). The LRIS spectral data were reduced using pypeit (Prochaska et al. 2020) and the resulting spectra are shown in Figure 4.

3. Results

The $H\alpha$ image of the M81 group is displayed in the left panel of Figure 2. This image has been continuum-subtracted with bright sources masked and has been smoothed with a Gaussian of 1.5 pixels FWHM. The $H\alpha$ emission traces extended ionized gas in the M81 group of galaxies and confirms structures that are already known in the field, such as the " $H\alpha$ cap" at ≈ 11 kpc from the disk of M82 (Devine & Bally 1999; Lehnert et al. 1999). It also reveals additional features that have not previously been detected in $H\alpha$. These include a ridge of emission south of the $H\alpha$ cap at ≈ 8 kpc from M82 along its minor axis, which has coincident x-ray emission (Lehnert et al. 1999). Also visible is an $H\alpha$ -emitting filament of gas at the eastern edge of the cap, which is aligned with the H I northern tidal stream (e.g., de Blok et al. 2018). This feature,

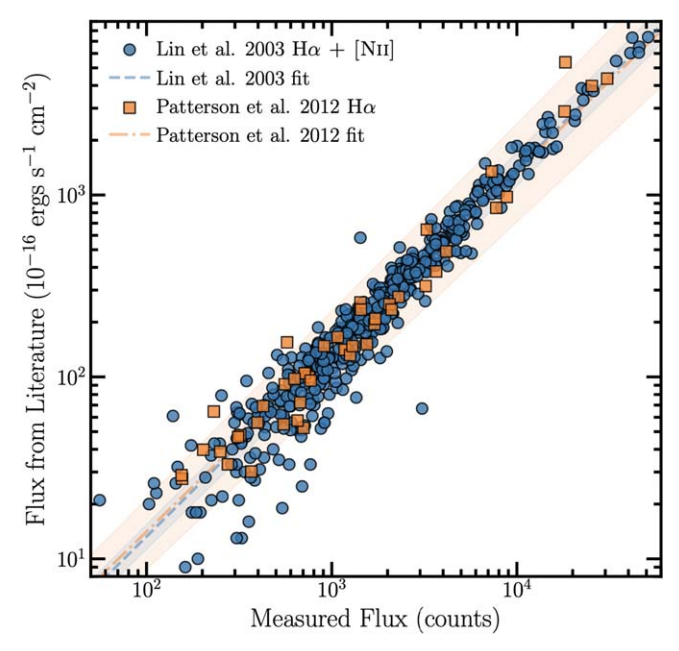


Figure 3. Flux calibration was carried out by comparing the ${\rm H}\alpha$ and [N II] emission flux of M81 H II regions measured in the pathfinder DSLM data to published values. The blue dashed/orange dashed-dotted line corresponds to a linear fit to published fluxes from Lin et al. (2003)/Patterson et al. (2012), where the shaded blue/orange region corresponds to 1σ uncertainty in the fit determined by bootstrapping and refitting the data to obtain a distribution of fit parameters.

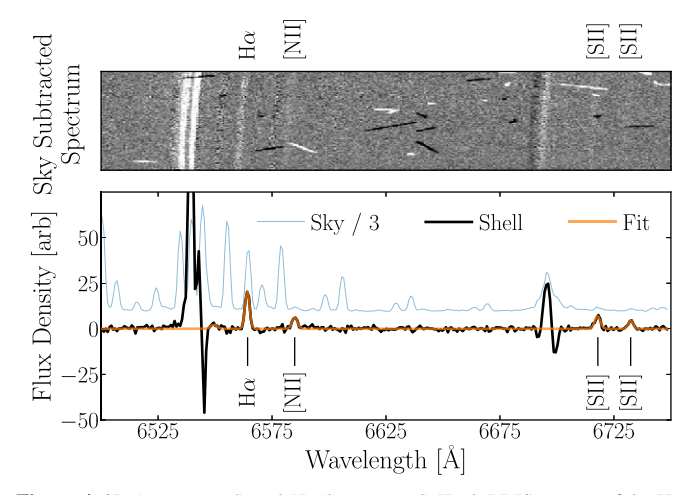


Figure 4. 2D (upper panel) and 1D (lower panel) Keck LRIS spectra of the ${\rm H}\alpha$ shell obtained to confirm the existence of the shell and provide basic parameters including radial velocity and relative [N II], [S II], and ${\rm H}\alpha$ line fluxes. LRIS spectra obtained at bluer wavelengths (3200–5400 Å) show nondetections of the [O II], [O III], and ${\rm H}\beta$ emission lines (not shown).

along with a unique large $H\alpha$ -emitting clump, is discussed in a companion letter (Pasha et al. 2021).

The most striking feature and the focus of this paper is a giant cloud of ionized gas in the field of M82 at the virial radius of the galaxy ($r_{\rm virial}$) $\approx 44^{+5}_{-1}$ kpc for a dynamical mass of M82 \sim (1 \pm 0.4) \times 10 10 M_{\odot} , adopting the R_{200} definition for the virial radius and cosmology with $H_0 = 70$ km s⁻¹ Mpc⁻¹; Greco et al. 2012). The inner edge of the shell of gas is \sim 30 kpc from M82 while the outermost edge is \sim 46 kpc from M82 in projection. The H α shell has an extremely large spatial extent: the projected length of the shell is \approx 0.8 with an average width of \approx 5.5, expanding to \approx 10.5 at the shell's widest part, with a total area of \approx 300 arcmin². At the

distance of M82, 3.66 Mpc (Tully et al. 2013), the shell has a physical size of $\approx\!55~\rm kpc\times5-10~\rm kpc$. The brightest region of the shell has an $\rm H\alpha$ surface brightness of $(6.5\pm0.3)\times10^{-18}$ erg cm $^{-2}$ s $^{-1}$ arcsec $^{-2}$ or approximately 1 Rayleigh. On average, the shell $\rm H\alpha$ surface brightness is $(1.95\pm0.15)\times10^{-18}$ erg cm $^{-2}$ s $^{-1}$ arcsec $^{-2}$ or roughly 0.5 Rayleigh. The total luminosity of the shell is $L_{\rm shell}\approx4.7\times10^{39}$ erg s $^{-1}$.

Figure 5 displays a comparison of the continuum-subtracted $H\alpha$ data (red colored regions) with the Dragonfly r-band continuum image (gray-scale background) and Very Large Array HI data (blue contours; de Blok et al. 2018). HI emission from the M81 group is shown in the left panel, where the velocity channels containing emission from Galactic sources have been removed and are shown separately in the right panel. Cirrus emission in the continuum data is clearly visible in the top right corner of the images (northwest of M82), but the spatial location and physical shape of the cirrus in the broadband images are distinct from the emission seen in the ${\rm H}\alpha$ image. There is no significant HI emission associated with the M81 group of galaxies at the location of the M82 shell, though there is one small spatially overlapping region at the southern edge of the shell. In both images, spatially coincident HI and $H\alpha$ emission have differing morphologies and velocities, which implies that these gaseous features are not related (this is further discussed below). The sensitivity limit of the H I map is 1.3×10^{19} cm⁻², therefore a nondetection at the location of the shell places an upper limit on the neutral gas mass of the shell of $\sim 10^7 M_{\odot}$ (using the quoted H I sensitivity of $\sim 10^4 M_{\odot}$ per 400 pc resolution element; de Blok et al. 2018).

The existence of the shell was confirmed spectroscopically with independent Keck LRIS observations. Figure 4 shows spectral data taken along a slit over the shell with the Keck LRIS longslit instrument. The spectra exhibit clear emission lines at the wavelengths of $H\alpha$, [N II], and [S II]. The emission lines in the spectrum were fit together using the Python packages astropy and specutils to determine a line-of-sight heliocentric velocity of -35.4 ± 4.3 km s⁻¹ for the shell. The LRIS spectra yield line ratios of [N II] $\lambda 6583/H\alpha = 0.340 \pm 0.003$ and [S II] $\lambda \lambda 6716$, $6731/H\alpha = 0.64 \pm 0.03$, where uncertainties are driven primarily by the sky subtraction. We estimate the metallicity of the gas (i.e., the oxygen abundance) from the logarithm of the [N II] $\lambda 6583$ $H\alpha$ ratio (the "N2" parameter; Denicoló et al. 2002) using the following equation from Pettini & Pagel (2004): $12 + \log(O/P)$ H) = $8.90 + 0.57 \times N2$. The N2 value derived from the spectral data yields $12 + \log(O/H) = 8.63$, which is about half solar metallicity (0.5 Z_{\odot} ; using abundances from Asplund 2005). However, if the source of ionization for the shell is shock-based, this metallicity estimate will be artificially skewed to higher values. We will return to the subjects of the ionization mechanism and accuracy of the metallicity estimate in Section 4.1.

A zoom-in comparison of the [N II] $\lambda 6583/H\alpha$ $\lambda 6563$ flux ratio in the vicinity of M82 and the shell is shown in Figure 6. Overlaid red shaded contours indicate levels of $H\alpha$ flux in the image. Regions with $H\alpha$ emission less than 1σ above the background level are removed from the ratio map. In the case of [N II], regions with signal-to-noise ratios <1 are replaced with the background level, yielding upper limits. The [N II]/ $H\alpha$ ratios detected in the shell range from as high as ≈ 1 along the inner edge of the shell down to [N II]/ $H\alpha$ \approx 0.16. This range is consistent with the [N II]/ $H\alpha$ ratio derived from the Keck LRIS spectra (0.34), which falls close to the middle of the range observed from the narrowband imaging (0.16–1). At the location

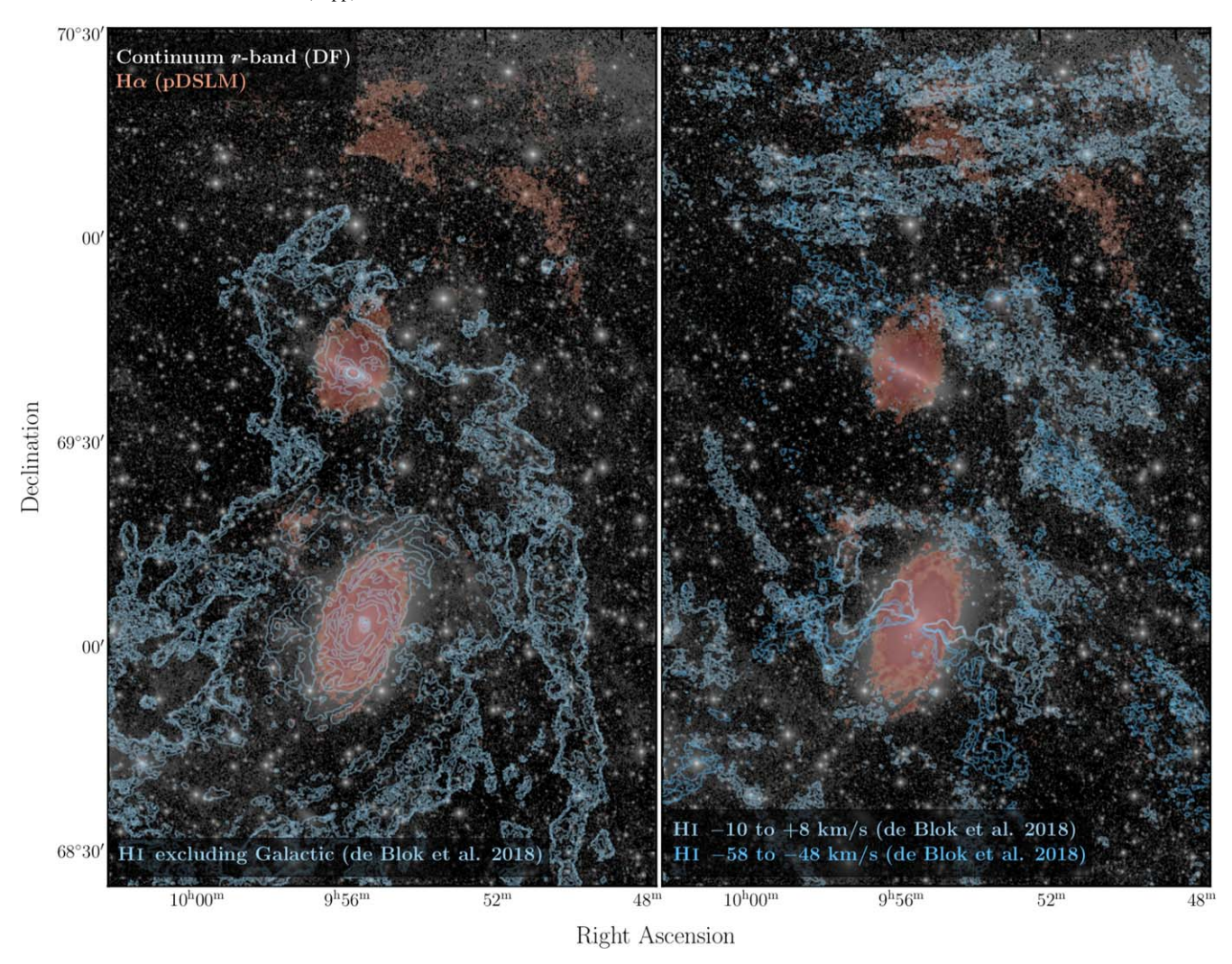


Figure 5. A composite image including regions of high signal-to-noise ratio in the pathfinder DSLM $H\alpha$ data shown in Figure 2 (red colored regions) with the r-band continuum image from the Dragonfly Telephoto Array (gray-scale background) and H I emission in the M81 group region (blue contours; de Blok et al. 2018). On the left, the H I emission is solely from neutral gas in the M81 group, excluding channels containing Galactic H I emission. On the right, the H I emission in velocity channels containing Galactic H I emission is shown. The H I emission is morphologically distinct from the H α shell.

of the LRIS slit, the [N II]/H α ratio from the narrowband imaging is [N II] $\lambda 6583/H\alpha = 0.39 \pm 0.09$, which is consistent with the LRIS ratio within the uncertainties. The large spread in [N II]/H α observed in the shell could be due to differing enrichment of the gas in the shell as a function of location, or due to differing ionization mechanisms (e.g., shocks and active galactic nuclei produce higher line ratios than H II regions due to the harder photoionizing radiation, e.g., Kewley et al. 2019).

We estimated the density of the shell from the [S II] $\lambda 6717/\lambda 6731$ line doublet ratio. The ratio between the two line intensities is 1.6 ± 0.1 , which places the cloud firmly in the low-density regime with an upper limit on the electron density of $n_e\lesssim 1~{\rm cm}^{-3}$ (Osterbrock & Ferland 2006). Another estimate for the average density in the shell can be made from the $H\alpha$ surface brightness measurement, assuming the shell is in thermodynamic equilibrium and case B recombination, with the equation $I_{\rm H}\alpha=8.7\times 10^{-8}E_m$ erg s⁻¹ cm² sr⁻¹ where E_m is the emission measure (Spitzer 1998). This yields $n_e\sim 1.4\times 10^{-4}(L_s/5~{\rm kpc})^{-1/2}(\eta/10^{-4})^{1/2}~{\rm cm}^{-3}$, where η is the volume filling factor of the shell (volume filling factors are typically between 10^{-6} and 10^{-1} for H II regions; Ho et al. 1997) and L_s is the line-of-sight length of the shell. The total mass of the shell using the n_e estimate from the $H\alpha$ surface

brightness is $M_{\rm H} \sim 5 \times 10^6 (L_s/5~{\rm kpc})^{1/2} (\eta/10^{-4})^{1/2}~M_{\odot}$. This mass is similar to that of a giant molecular cloud and below the detection limit of the de Blok et al. (2018) H I map.

4. The Origin of the H α Shell

As discussed earlier, the M81 group of galaxies is an extremely active group of galaxies, yielding many possibilities for the origin of the shell. It could be gas lifted from the disk of M82 by the powerful central starburst (as originally argued for the origin of the $H\alpha$ cap) or gas falling in onto the galaxy for the first time from the intergalactic medium. The umbrella-like shape of the cloud centered on the location of M82 and in line with its minor axis strongly suggests an origin or excitation mechanism related to the starburst of M82. The giant shell could be tidally stripped from the group of galaxies similarly to the widespread tidal features traced by HI emission, which were produced by close passages between M81 and M82, the last of which was 200-300 Myr ago (e.g., Cottrell 1977; Yun et al. 1993, 1994). The similarities of size and position between the neutral and ionized gas can be seen in Figure 5. Alternatively, the cloud could be a chance projection of gas in the Galaxy and be unrelated to the M81 group. We discuss

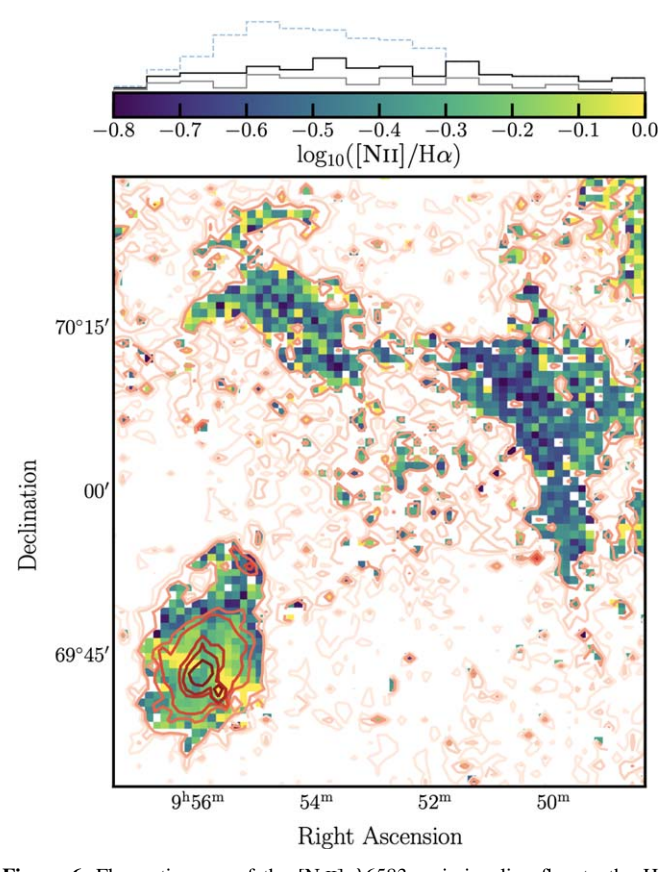


Figure 6. Flux ratio map of the [N II] $\lambda 6583$ emission line flux to the $H\alpha$ $\lambda 6563$ emission line flux in the vicinity of M82 and the shell. The map is log-scaled between -0.8 and 0. A contour map of $H\alpha$ data is superimposed (red shaded contours). Regions of low signal-to-noise ratio in the H α emission line are removed from the ratio map, while regions with low signal-to-noise ratio in the [N II] emission line are replaced with the sky background level as upper limits. A histogram of the number counts of [N II]/H α values in the shell is shown above the color bar. The blue dashed lines include regions that use upper limits for the [N II] values, whereas the black and gray solid lines do not include such regions and have applied a 1σ and 2σ cut on the $H\alpha$ data, respectively.

constraints on the origins of the $H\alpha$ shell based on the viability of ionization mechanisms, along with the mass, metallicity, and velocity of the shell.

4.1. Ionization Mechanism of the Shell

The $H\alpha$ emission from the shell could be produced through photoionization (e.g., by the local or global ultraviolet ionizing background (UVB), active galactic nuclei, starburst ionizing radiation, or young OB stars) or shock ionization of the gas. The shell could also be a light echo of line emission from a past period of bright emission from a nearby source, such as a peak of starburst emission from M82. We start by determining the photon ionizing flux required to produce the observed level of $H\alpha$ emission. We can then compare that to the photon flux available whether the cloud is positioned within the M81 group or within the Galaxy. Assuming ionization equilibrium and case B for optical recombination emission, the number of ionizing photons, Q_{H^0} , for the optical line recombination emission is given by Osterbrock & Ferland (2006):

$$Q_{\rm H^0} = \frac{L_{\rm H\alpha}}{h\nu_{\rm H\alpha}} \frac{\alpha_{\rm B}}{\alpha_{\rm H\alpha}^{\rm eff}},\tag{1}$$

where $L_{{\rm H}\alpha}$ is the luminosity of the H α emission, $\alpha_{\rm B}$ is the recombination coefficient for case B H α emission (2.59 × 10^{-13} cm³ s⁻¹ at temperature $T=10^4$ K; Osterbrock & Ferland 2006), and $\alpha_{{\rm H}\alpha}^{\rm eff}$ is the H α effective recombination coefficient (11.7 × 10^{-14} cm³ s⁻¹ at temperature $T=10^4$ K and electron density $n_e\approx 1$ cm⁻³; Spitzer 1998). Assuming that the cloud is roughly spherical, we can directly estimate the photoionization rate and compare it with estimates for the UVB. Note that adjustments to this geometry (e.g., cylindrical or planar) result in an estimate of the same order of magnitude (e.g., Donahue et al. 1995). Assuming a power-law approximation for the photoionization cross section (Osterbrock & Ferland 2006) yields the following equation for the photoionization rate, Γ :

$$\Gamma = \frac{4\pi A_0}{h} \frac{J_0}{\beta + 3},\tag{2}$$

where h is Planck's constant, A_0 is the photoionization cross section at the Lyman limit, $J_0(\nu)$ is the source of ionizing photons, and β is the power-law coefficient for $J_0(\nu)$ (commonly assumed to be 1.8 for the redshift z=0 UVB; e.g., Adams et al. 2011). Together, Equations (1) and (2) yield an estimate for the ionizing source of photons to have a photoionization rate $\Gamma \approx 2 \times 10^{-12} \ \mathrm{s}^{-1}$. This is two orders of magnitude higher than the current estimate for the global UVB at redshift z=0 (e.g., Fumagalli et al. 2017), indicating that there needs to be an additional source of ionization for the shell

If the shell is part of the M81 group, alternative possibilities for ionizing the shell are photoionization by high-energy photons from the starburst in M82 or shock ionization. We first consider whether it is viable for the ionizing photons from the starburst in M82 to ionize the gas in the shell and produce the observed $H\alpha$ emission. The number of $H\alpha$ photons from the shell is $\approx 1.56 \times 10^{52}$ photons s⁻¹ and applying Equation (1) yields the required number of ionizing photons to produce this emission to be $\approx 3.5 \times 10^{52}$ photons s⁻¹. The ionizing flux from the M82 starburst is $\sim 10^{54}$ photons s⁻¹ (McLeod et al. 1993, and references therein), and the fraction intercepted by the shell would be $\approx 3\%$ –23% of that, where the line-of-sight width of the shell is estimated to range between its transverse height (\approx 9') and length (\approx 55'). For shell line-of-sight widths ranging from $\approx 9'$ to 55', the required escape fraction is therefore \sim 95%–20%. This escape fraction is significantly higher than that observed in the Galaxy or in dwarfs (\sim 6% and \sim 3%, respectively; e.g., Bland-Hawthorn & Maloney 1999; Zastrow et al. 2011; Barger et al. 2012). This implies that photoionization of the shell from the M82 starburst may be possible only if the superwinds from the M82 starburst cleared the field of M82, or if there is anisotropic radiation from the starburst with flux focused along the minor axis of M82. The shell emission could be an "ionization light echo" produced by ionizing photons from a peak in the M82 starburst that occurred $\gtrsim 2 \times 10^5$ yr ago and has since dropped off. Förster Schreiber et al. (2003) determined that there were peaks in starburst activity $(5-10) \times 10^6$ yr ago, which lasted a few million years and produced ionizing flux at least an order of magnitude greater during its peak than is currently observed. The recombination timescale of the hydrogen atoms for the estimate of electron density in the shell of $n_e \sim 10^{-4} \text{ cm}^{-3}$ is $\sim 10^9 \text{ yr}$, so one would expect to still see H α emission from ionization

that occurred $\sim 10^7$ yr ago. Accounting for this increase would ease the requirements on the high escape fraction from M82 to photoionize the shell.

Shocks from the accretion of gas onto the M81 group or M82 halo or shocks produced by the M82 superwinds incident upon the shell could also play a large role in the ionization of the gas. The disruption of an infalling cloud itself may also produce shock emission (Bland-Hawthorn et al. 2007). The higher end of the range of [N II]/H α ratios observed in the shell ([N II]/H $\alpha \ge 0.6$) implies a harder radiation field than that produced by normal star-forming regions (e.g., Kewley et al. 2019), which suggests that shock ionization must play a role in the shell. The H α cap is thought to have been ionized through both slow and fast shocks from the M82 superwinds with shock velocities of \approx 50 and 800 km s⁻¹, respectively; perhaps a similar situation is occurring in the shell (Matsubayashi et al. 2012; Lehnert et al. 1999). The higher end of $[N II]/H\alpha$ ratios from the narrowband images ([N II]/H $\alpha \approx 0.3$ –1) and [S II]/ ${
m H}lpha$ ratios from the spectra are consistent with shocks of velocity between 80 and 350 km s⁻¹ into gas of solar (Z_{\odot}) to double solar $(2 Z_{\odot})$ metallicity based on the MAPPINGS III fast shock models from Allen et al. (2008, see their Figure 21) and slow shock models of Rich et al. (2010) and Raymond (1979). The lower end of $[NII]/H\alpha$ values found in the shell ([N II]/H $\alpha \approx 0.16$ –0.4) is consistent with shocks into gas with metallicity of $\approx 0.25 Z_{\odot}$ (without further line information the shock velocity in this case cannot be narrowed down; Allen et al. 2008). The line ratios measured in the spectra have small line widths, consistent with velocity dispersion $\leq 50 \,\mathrm{km \ s^{-1}}$, which suggests that slow shocks rather than fast shocks are responsible for the ionization of the shell. The range of [N II]/ $H\alpha$ ratios observed in the shell may be produced by a range of shock velocities across the shell (e.g., a higher shock velocity at the northeastern edge of the shell where the emission is brightest, which is in line with the superwind outflow from M82). In order to confirm whether a shock is ionizing the gas in the shell and to pinpoint the shock velocities, follow-up observations are required. For example, deeper spectroscopy targeting the optical or UV emission lines (such as the [N II]/ $H\alpha$ and [O III]/ $H\beta$ line ratios) will allow better constraints on the required shock velocity. Optical line ratios such as [O III] $\lambda 5007/[O~III]~\lambda 4363$ and [N II] $\lambda 6583/[N~II]~\lambda 5755$ and X-ray observations can also be used to determine the temperature of the gas, which is related to the shock speed.

4.2. Is the Shell Part of the M81 Group or the Galaxy?

The morphology, size, and position of the $H\alpha$ shell strongly suggest that it is associated with the M82 galaxy, but due to the possibility of a chance projection of Galactic clouds with the M81 group it is worth considering the possibility that the shell is associated with the Milky Way galaxy. Associations between gaseous features and galaxies nearby in projection can often be made by comparing the radial velocities of the gas and of the galaxies (e.g., see analogous arguments made by Watkins et al. 2018, in their discovery of a gas cloud near M51). Since the M81 group of galaxies is near rest velocity with respect to the Milky Way in this case the velocity of the cloud is not enough to differentiate between an association with the Galaxy and one with the M81 group. The radial velocities of M81 and M82 are \approx -15 km s⁻¹ and \approx 210 km s⁻¹, respectively (e.g., Yun et al. 1994; Beck et al. 1978; McKeith et al. 1993), while the velocity

of the shell is measured to be $\approx -35 \, \mathrm{km \ s^{-1}}$ from the LRIS spectra ($\approx -250 \, \mathrm{km \ s^{-1}}$ with respect to M82). The M82 H α cap contains gas at velocities between -250 and $250 \, \mathrm{km \ s^{-1}}$ with respect to the systematic velocity of M82 (Devine & Bally 1999) while the radial velocity of the H I content in the M81 group ranges between -270 and $320 \, \mathrm{km \ s^{-1}}$ (e.g., de Blok et al. 2018). The radial velocity of the shell is consistent with both of these velocity spreads.

No extensions to the shell of equivalent signal-to-noise ratio are apparent in the H α pathfinder DSLM imaging shown in the right panel of Figure 2, suggesting that the shell is a condensed structure and not part of a larger Galactic stream of gas. Highlatitude clouds in the Milky Way, such as high-velocity clouds (HVCs), are defined by their neutral gas content. There is a lack of HI in the region of the shell, which is unusual for HVCs. The nearest HVCs to the M81 field are Complex C and Complex A, which skirt the region of the M81 group. The HVCs and the H α shell are spatially separated in projection by an angular distance of more than 4° (Westmeier 2018). In addition, the velocities measured from H α emission and H I in Complexes A and C are between -165 and -180 km s⁻¹ and -111 ± 2 km s⁻¹, respectively (Tufte et al. 1998). This is significantly different at the 10σ level from the measured H α velocity of the shell ($-35.4 \pm 4.3 \text{ km s}^{-1}$). However, catalogs of known HVCs are not necessarily comprehensive, since emission sources with velocities within the "deviation velocity" (e.g., $\pm 50 \text{ km s}^{-1}$ about the velocity of the Galactic disk) are often not included when searching for HVCs. We have inspected this velocity gap using the de Blok et al. (2018) H I emission measurements covering the M81 group, which contain channel maps from -58 to -48 km s⁻¹ and -10 to +8 km s⁻¹ that are associated with Galactic emission (all other channels are determined to be associated with the M81 group). The H I emission within those channels is compared to the H α emission in the right panel of Figure 5, in which the H I and H α data are plotted as blue contours and red shading, respectively. The morphology of the HI gas at these velocities is distinct from the shell, with filamentary H I emission spanning the field of view. Spatially coincident H I emission does not appear to be coherent with the $H\alpha$ shell, differing in both shape and size.

Another indicator of whether the shell could be part of the Galaxy is if there is a viable ionization mechanism that could produce the observed emission. If the shell is in the Galaxy, the expected photoionization mechanism would be either young OB stars (such as in H II regions) or the local UV background. In Section 4.1, we showed that the global UVB would not be enough to ionize the cloud such that it produces the observed surface brightness of $H\alpha$ emission. Additionally, we see no evidence for bright ionizing stars in the broadband data, or for ionization from localized sources within the cloud—the cloud appears to be uniformly illuminated at the resolution scale of our data. The image pixel scale corresponds to ≤ 0.02 pc per pixel for radial distances ≤ 2 kpc, so star-forming clumps in the cloud would be resolved if the cloud was in the Galactic disk. In addition, the high line ratios argue against ionization from young stars, as discussed in Section 4.1.

Based on the shell's morphology, velocity, line ratios, and stellar associations, we thus conclude that the shell is most likely associated with the M81 group rather than being an interstellar or high-galactic-latitude cloud in the Galaxy.

4.3. Is the Gas Tidally Stripped from M81 or M82?

The M81 group of galaxies began interacting about 1 Gyr ago, with the closest encounter occurring about 0.3 Gyr ago, during which gas was tidally stripped from the galaxies and redistributed across the field of the group (e.g., Yun et al. 1994; Mayya et al. 2006, and references therein). If the shell was produced during the interactions, one would expect the spatial and dynamic properties of the shell to match those of the HI gas tidally stripped from the galaxies (see, e.g., simulations of Yun et al. 1994). Inspection of the channel maps from de Blok et al. (2018, their Figure 2) shows that there is tidally stripped H I gas with radial velocities ranging from −260 to 320 km s⁻¹, but the spatial distribution of the gas varies greatly across the range of velocities. HI gas with radial velocity below 20 km s⁻¹ is only located at the position of M81 and southward, with no gas north of decl. $\approx 60^{\circ}$. The velocity of the H I gas at the same decl. as the shell ($\delta \approx 70^{\circ}$) is $\gtrsim 160 \text{ km s}^{-1}$, which is inconsistent with our derived shell velocity of $\approx -35 \,\mathrm{km \ s}^{-1}$ (de Blok et al. 2018; Yun et al. 1994; Chynoweth et al. 2008). It therefore seems unlikely that the $H\alpha$ shell is an ionized extension of the HI gas that was tidally stripped, implying either a separate stripping event or a different mechanism for the origin of the shell. A separate tidal stripping event seems unlikely because that would be expected to produce HI in addition to HII. Further simulations of the M81 group interactions going back farther in the history of the group (e.g., \gtrsim 1 Gyr) are required in order to determine whether a separate tidal event could have formed the $H\alpha$ shell.

4.4. Is the Shell Gas Lifted from the Disk of M82?

Could the shell be composed of gas that was lifted from the disk of M82 by the starburst, as was thought to have happened to create the H α cap (e.g., Devine & Bally 1999)? If the gas was pushed by superwinds from the starburst, it would take \sim 50 Myr to reach its current location, assuming a wind velocity of $\approx 800 \text{ km s}^{-1}$ on average (Lehnert et al. 1999). The epochs of peak starburst activity were modeled by Förster Schreiber et al. (2003) to have occurred \sim 10 Myr ago followed by a second starburst ∼5 Myr ago. If gas was lifted from the disk of M82 to the current position of the shell, an additional starburst \$\geq 50 Myr ago is needed, assuming an average wind velocity of $\lesssim 800 \text{ km s}^{-1}$. This event is not predicted by models of star formation in M82, which model star formation up to \sim 100 Myr ago (Förster Schreiber et al. 2003; Yao 2009, and references therein). It is possible that the tidal interactions of M81 and M82 about 250 Myr ago produced a starburst in M82, which provided the energy to blow out the gas to the location of the shell. The durations of the starbursts are expected to be a few million years each (Förster Schreiber et al. 2003), so assuming a supernova energy production rate of $\sim 10^{43}$ erg s⁻¹ (Chevalier & Clegg 1985), the total energy available ($\sim 10^{56}$ erg) would be more than that required to lift the mass of the shell from the disk of M82 to its current position ($\lesssim 10^{54}$ erg). This activity is not merely gravitational but also ballistic, requiring enough force against the ambient medium to raise the gas to the shell position. We carry out a back-of-the-envelope calculation to determine whether a blast wave could move the gas through ambient medium of density $n_{\rm H} \approx 0.01~{\rm cm}^{-3}$. This number density corresponds to the average column density in the M81 group at a few tens of kiloparsecs from the galaxies in the HI measurements of de Blok et al. (2018) and assumes a lineof-sight width of 5 kpc. The resulting Sedov–Taylor solution (e.g., Truelove & McKee 1999) requires an energy input from the M82 superwind according to the following relation: $L \approx 2 \times 10^{41} \, \mathrm{erg \ s^{-1}} (v/70 \, \mathrm{km \ s^{-1}})^3 (R/44 \, \mathrm{kpc})^2 (n/0.01 \, \mathrm{cm^{-3}})$. This energy can be supplied by the supernova energy production rate in M82 ($\sim 10^{43} \, \mathrm{erg \ s^{-1}}$; Chevalier & Clegg 1985). While basic energetics arguments allow the possibility of the gas being blown out to the radius of the M82 shell, the question of whether the gas would survive within the hot wind from M82 remains.

Kelvin–Helmholtz and Rayleigh–Taylor instabilities have been shown to shred cold gas clouds entrained in winds within a timescale of ~1 Myr (e.g., Cooper et al. 2009) but recent analytic work and simulations have determined potentially viable mechanisms for the stable production and maintenance of cold gas in a hot wind (e.g., Scannapieco & Brüggen 2015; Thompson et al. 2016; Gronke & Oh 2018; Sparre et al. 2019; Schneider et al. 2020; Fielding & Bryan 2022; Gronke et al. 2022). In particular, recent simulations have shown that cold gas may be produced in the mixing layer between the cold cloud and hot (laminar) wind (Gronke & Oh 2018) as long as the cold clouds are large enough (e.g., $R_{\rm cloud} \gtrsim 1-150$ pc; Gronke & Oh 2018; Sparre et al. 2019). Taking into account a filling factor of 10^{-4} , individual "cloudlets" within the shell would take up a total volume of $\sim 500^3$ pc³. This size is above the minimum needed for survival predicted by these simulations, but the initial number of cloudlets would play an important role in determining their actual size and survivability. Cool clouds are prone to fragmentation (e.g., McCourt et al. 2018; Sparre et al. 2019), and large clouds in a turbulent hot medium are predicted to be shredded into many "droplets" spread out over a large area (Gronke et al. 2022). If this is the case for the shell, perhaps the shell started out with a smaller volume and was dispersed in a turbulent wind. Further studies with longer timescales and larger box sizes, and with additional physics (such as magnetic fields, cosmic rays, etc.), are required to confirm whether this could be the process that created the $H\alpha$ shell.

In addition to gas being lifted from the disk, it is possible the superwind swept up existing gas surrounding M82. A potential scenario is that the northern surroundings of M82 may also have originally been filled with tidally disrupted H I gas at similar levels to the H I observed in the southeast, and the M82 superwind ionized and pushed the tidally disrupted gas out to the location of the H α shell. The dynamics of the shell would require the superwind to have pushed the gas along the line of sight toward the observer, implying that in the past there was a stronger radial component to the superwind than has been measured (e.g., Shopbell & Bland-Hawthorn 1998). In addition to more detailed simulations of the tidal disruption, further comparisons between the metallicity properties of the gas in the shell and the tidally disrupted H I gas would be helpful to determine whether they have the same origin.

4.5. Is the Gas Infalling from the Intergalactic Medium?

If the gas in the shell is infalling from the intergalactic medium (IGM), the shell would need to have dynamics and metallicity consistent with an inflow. The H α shell has a relative radial velocity $\lesssim 20 \, \mathrm{km \ s^{-1}}$ with respect to M81, which has a systemic velocity of $v_{\mathrm{M81}} \approx -15 \, \mathrm{km \ s^{-1}}$ (Yun et al. 1994). The escape velocity of M81 at the projected distance of the shell is $v_{\mathrm{esc},\mathrm{M81}} \approx 250 \, \mathrm{km \ s^{-1}}$, so the shell is likely bound to the group and could be falling into its center of mass. The shell

has a large relative velocity with respect to M82 (\approx 250 km s⁻¹), which is greater than the escape velocity of M82 ($\nu_{\rm esc,M82}\approx$ 50 km s⁻¹). Consequently, the mass of M82 alone would not gravitationally capture the shell. If the shell is infalling, the gas likely will either end up as part of the intragroup medium or accrete onto M81 rather than M82.

The IGM is expected to have on average a metallicity of ${\sim}0.1\,Z_{\odot}$ in the local universe, though there is a large variation of metallicities predicted in simulations due to poor mixing of the IGM (e.g., a spread of metallicity of $Z_{\rm IGM}/Z_{\odot} \sim 0.001$ –1; Shull et al. 2012). If the gas is infalling from the IGM for the first time, its metallicity should fall within this range. As the [N II]/H α ratio in the shell is likely boosted by shock emission, it is difficult to accurately determine an estimate of the metallicity in the gas. The [N II]/H α ratios in the shell are consistent with [N II]/H α ratios in the MAPPINGS III shock models for metallicities of ${\sim}0.2$ –2 Z_{\odot} (see, e.g., Figure 21 from Allen et al. 2008, and discussion in Section 4.1). Additional line information would help to further constrain the metallicity estimate.

As the position of the shell is well within the virial radius of the M81 group (at about $R_{\rm vir}/2$ of M81; see Figure 2), one potential scenario could be that intragroup gas was originally pressure-supported by gas in the group, then the M82 superwinds removed gas along the northern minor axis of M82, which allowed the gas to freefall inwards and shock at a position closer the galaxies within the virial radius of the group. Accretion shocks at or within the virial radius are expected to occur for halos of the sizes of the M81 group ($\sim 10^{12} M_{\odot}$; Karachentsev & Kashibadze 2006; Birnboim & Dekel 2003). Thus the infalling gas may have experienced an accretion shock instead of (or in addition to) being shocked by the M82 superwind.

4.6. Composite Origin Scenario

The final scenario we consider is one in which the M82 superwind entrained hot gas from the M82 disk and raised it to the position of the shell, where it shocked and mixed with the intragroup gas, ionizing the in situ gas and producing the H α emission we observe. Along with introducing density perturbations that seeded the precipitation of the circumgalactic gas (as predicted in simulations, e.g., Esmerian et al. 2021), the entrained gas in the superwind could have mixed with the in situ intragroup gas and enriched it. The low velocity dispersion from the line widths of the spectral data belies this theory because one would expect the mixing of the windblown gas with the intragroup gas to introduce turbulence into the medium. As such, perhaps the shell was enriched so far in the past that other relics of that event have long since vanished such as through an early tidal event or through extended superwind events. More modeling is required to confirm or disprove these possibilities.

5. Comparison with Similar Objects from Literature

Similar structures have been reported previously, such as "Hanny's Voorwerp" near the spiral galaxy IC 2497 (Lintott et al. 2009) and a cloud in the halo of M51 (Watkins et al. 2018). These two gaseous structures were also discovered in H α emission and are notably closer in projection to their associated galaxies, with projected distances of 25 kpc and 32 kpc, respectively. These distances place the clouds well

within the virial radii of their host galaxies whereas the M82 shell is at the virial radius of M82 (i.e., the outer edge of the CGM; Tumlinson et al. 2017), making it likely to be an intragroup cloud.

In addition, many H α -emitting objects have been found with close association to galaxies (Bait et al. 2019, and references therein). Most of these structures appear to have tidal origins and many have an optical counterpart. We do not detect a continuum emission counterpart to the H α shell, though the presence of significant Galactic cirrus in the field makes the detection difficult and might mask the presence of a lowsurface-brightness stellar counterpart to the shell. In the stellar density maps of the red giant branch (RGB) of Smercina et al. (2020), the whole field presented here is filled with stars. Inspection of their maps reveals no statistically significant overdensity of RGB stars at the location of the H α shell. In any case, no known or candidate dwarf galaxies are coincident with the shell location (Chiboucas et al. 2009; Okamoto et al. 2019). Deep follow-up is required to determine whether a significant stellar counterpart exists. If a significant metal-poor stellar counterpart were found it would suggest that the shell could be a dispossessed "old disk" component of M82, which Sofue (1998) theorizes may have been ripped off M82 during its tidal interactions ~1 Gyr ago and has not yet been observed. Though ionization and origin mechanisms vary between these $H\alpha$ -emitting clouds, the relative velocities of the $H\alpha$ structures and their associated galaxies range from 150 to 400 km s⁻¹ (Bait et al. 2019), which is consistent with the velocity difference observed between M82 and the H α shell and with an M81 group association for the shell.

6. Summary and Conclusion

Deep H α imaging of the M81 group of galaxies with a novel upgrade to the Dragonfly Telephoto Array, a pathfinder version of the Dragonfly Spectral Line Mapper, has revealed a host of low-surface-brightness gaseous structures within the group. One significant structure is a colossal H α -emitting "shell" of gas, over 0°.8 in length, ≈40 kpc from the M82 galaxy in projection along its minor axis, i.e., at and potentially beyond the virial radius of the galaxy. We argue that the shell is part of the M81 group of galaxies due to its morphology, velocity, and potential sources of ionization (rather than being a chance projection of Galactic gas with the M81 group). In order to ionize the gas seen in the shell, an additional source of ionization to the global UVB is required. We show that the shell is consistent with being shock-ionized, either through incident superwinds from the M82 starburst or through accretion shocks as the gas is falling into the group of galaxies. While the gas in the shell could have a tidal origin, the shell does not have similar velocity or spatial overlap with the extensive tidally stripped HI gas in the group, which one would expect to see if the gas was tidally stripped. We consider whether the gas could be M82 disk gas entrained in the superwind produced by the M82 starburst or tidally stripped gas that was caught up in the superwind, but the question remains whether the cold gas would be expected to survive long enough to reach the location of the shell. Alternatively, the shell could have an external origin, with gas falling in from the intergalactic or intragroup medium. With a radial velocity much less than the escape velocity of M81, the shell is likely bound to the group. Further analysis of the M82 H α shell, including X-ray, UV, and/or deep visible spectral observations

to pinpoint the ionization source of the gas, is required to determine its origin.

Imaging of the M81 group of galaxies with the pathfinder DSLM serves as a test case for deep wide-field ${\rm H}\alpha$ imaging of large-scale gaseous structures around nearby galaxies. This work foreshadows investigations of other nearby galaxies with an upcoming 120-lens Dragonfly Spectral Line Mapper that will begin taking data in 2022. The DSLM upgrade is based on the pathfinder that was used to collect the data presented here (further details on the DSLM instrument are described in S. Chen et al., in preparation). DSLM will have $40\times$ the collecting area of the pathfinder and will reach the limits presented here in under one hour.

This work was benefited greatly from conversation and correspondence with Crystal Martin, Joss Bland-Hawthorn, Chris Matzner, and Natasha Förster-Schreiber, as well as through useful feedback from the anonymous reviewer. We thank you for your comments and guidance. Many thanks to the staff at New Mexico Skies Observatories who provided great assistance with the instrument deployment, testing, and data collection. The work done by D.L. for this paper was supported through grants from the Ontario government. We are thankful for contributions from the Dunlap Institute (funded through an endowment established by the David Dunlap family and the University of Toronto), the Natural Sciences and Engineering Research Council of Canada (NSERC), and the National Science Foundation (NSF), without which this research would not have been possible. S.D. is supported by NASA through Hubble Fellowship grant HST-HF2-51454.001-A awarded by the Space Telescope Science Institute, which is operated by the Association of Universities for Research in Astronomy, Incorporated, under NASA contract NAS5-26555.

Facility: Dragonfly Telephoto Array; pathfinder Dragonfly Spectral Line Mapper; Keck LRIS

Software: astropy (Astropy Collaboration et al. 2013), source-extractor (Bertin & Arnouts 1996), pypeit (Prochaska et al. 2020), iraf (Tody 1986)

Appendix DSLM Data Reduction with DFReduce

The data reduction pipeline for Dragonfly data is described in detail in Danieli et al. (2020) and Zhang (2021), and we refer the interested reader to these publications for details on the data reduction procedures. In this Appendix, we summarize the basic steps and any differing procedures for narrowband data reduction. The narrowband and broadband data were reduced using the DFReduce package. While the reduction procedures for both data sets were similar, they were reduced separately due to the differing pixel scales in the CCD cameras used by the 48-lens Dragonfly and the pathfinder DSLM.

The images were dark-subtracted and flat-fielded. For the narrowband data, flat-fielding was carried out using master flats created from flats at the same tilt and pointing as the data. After dark subtraction and flat-fielding, the data were passed through a series of image quality checks to throw out "bad" data frames. These checks included limits on the FWHM, ellipticity, and number of point sources, as well as removing frames that were determined to be off-target by more than 1.5.

At this point, the frames went through the first round of sky subtraction. The background sky in each frame was separately modeled with a third-order polynomial and subtracted from each image. Sky subtraction for emission lines is often a large source of error due to the strength of sky lines relative to astrophysical emission lines from diffuse gas; by masking and fitting a low-order polynomial across each image, we removed large-scale emission on scales of \sim 0°.5. The frames were then registered to align them onto the same grid. The average magnitude zero-point level of the point sources in each frame was then calculated, and frames with a difference in zero-point of greater than 0.1 mag from the median zero-point of all frames taken by the same camera were rejected. For both the narrowband and the r broadband data, the zero-point level was calculated by comparing the magnitude in the data frames to the r-band magnitude from The AAVSO Photometric All-Sky Survey catalog. This proved suitable for rejecting nonphotometric frames for all the data.

After rejection of bad frames, the images were stacked together, taking the median of each pixel value to create median coadds separately for the narrowband and broadband data. All the accepted frames then went through another round of data reduction, repeating all the steps above up to registering the frame, but with one change: during the sky subtraction, the median coadd was used to create a mask for all point sources to create the sky model to better subtract the sky from the data. After a final registration, the data were combined into average stacks to form final science images in $H\alpha$, [N II], g, and r, with a common pixel scale of 2."1 per pixel.

ORCID iDs

```
Deborah Lokhorst https://orcid.org/0000-0002-2406-7344
Roberto Abraham https://orcid.org/0000-0002-4542-921X
Imad Pasha https://orcid.org/0000-0002-7075-9931
Pieter van Dokkum https://orcid.org/0000-0002-8282-9888
Seery Chen https://orcid.org/0000-0002-4175-3047
Tim Miller https://orcid.org/0000-0001-8367-6265
Shany Danieli https://orcid.org/0000-0002-1841-2252
Johnny Greco https://orcid.org/0000-0003-4970-2874
Jielai Zhang https://orcid.org/0000-0001-5310-4186
Allison Merritt https://orcid.org/0000-0001-9467-7298
Charlie Conroy https://orcid.org/0000-0002-1590-8551
```

References

```
Abraham, R. G., & van Dokkum, P. G. 2014, PASP, 126, 55
Adams, J. J., Uson, J. M., Hill, G. J., & MacQueen, P. J. 2011, ApJ, 728, 107
Allen, M. G., Groves, B. A., Dopita, M. A., Sutherland, R. S., & Kewley, L. J.
   2008, ApJS, 178, 20
Asplund, M. 2005, ARA&A, 43, 481
Astropy Collaboration, Robitaille, T. P., Tollerud, E. J., et al. 2013, A&A,
Bait, O., Wadadekar, Y., & Barway, S. 2019, MNRAS, 485, 428
Barger, K. A., Haffner, L. M., Wakker, B. P., et al. 2012, ApJ, 761, 145
Beck, S. C., Lacy, J. H., Baas, F., & Townes, C. H. 1978, ApJ, 226, 545
Bertin, E., & Arnouts, S. 1996, A&AS, 117, 393
Birnboim, Y., & Dekel, A. 2003, MNRAS, 345, 349
Bland-Hawthorn, J., & Maloney, P. R. 1999, ApJL, 510, L33
Bland-Hawthorn, J., Maloney, P. R., Stephens, A., Zovaro, A., & Popping, A.
   2017, ApJ, 849, 51
Bland-Hawthorn, J., Sutherland, R., Agertz, O., & Moore, B. 2007, ApJL,
   670, L109
Chevalier, R. A., & Clegg, A. W. 1985, Natur, 317, 44
Chiboucas, K., Karachentsev, I. D., & Tully, R. B. 2009, AJ, 137, 3009
Chynoweth, K. M., Langston, G. I., Yun, M. S., et al. 2008, AJ, 135, 1983
Cooper, J. L., Bicknell, G. V., Sutherland, R. S., & Bland-Hawthorn, J. 2009,
   ApJ, 703, 330
Cottrell, G. A. 1977, MNRAS, 178, 577
Danieli, S., Lokhorst, D., Zhang, J., et al. 2020, ApJ, 894, 119
de Blok, W. J. G., Walter, F., Ferguson, A. M. N., et al. 2018, ApJ, 865, 26
```

```
de Mello, D. F., Smith, L. J., Sabbi, E., et al. 2008, AJ, 135, 548
Denicoló, G., Terlevich, R., & Terlevich, E. 2002, MNRAS, 330, 69
Devine, D., & Bally, J. 1999, ApJ, 510, 197
Donahue, M., Aldering, G., & Stocke, J. T. 1995, ApJL, 450, L45
Esmerian, C. J., Kravtsov, A. V., Hafen, Z., et al. 2021, MNRAS, 505, 1841
Fielding, D. B., & Bryan, G. L. 2022, ApJ, 924, 82
Förster Schreiber, N. M., Genzel, R., Lutz, D., & Sternberg, A. 2003, ApJ,
Fumagalli, M., Haardt, F., Theuns, T., et al. 2017, MNRAS, 467, 4802
Gilhuly, C., Hendel, D., Merritt, A., et al. 2020, ApJ, 897, 108
Greco, J. P., Martini, P., & Thompson, T. A. 2012, ApJ, 757, 24
Gronke, M., & Oh, S. P. 2018, MNRAS, 480, L111
Gronke, M., Oh, S. P., Ji, S., & Norman, C. 2022, MNRAS, 511, 859
Harmsen, B., Monachesi, A., Bell, E. F., et al. 2017, MNRAS, 466, 1491
Ho, L. C., Filippenko, A. V., & Sargent, W. L. W. 1997, ApJ, 487, 579
Karachentsev, I. D., & Kashibadze, O. G. 2006, Ap, 49, 3
Kewley, L. J., Nicholls, D. C., & Sutherland, R. S. 2019, ARA&A, 57, 511
Lehnert, M. D., Heckman, T. M., & Weaver, K. A. 1999, ApJ, 523, 575
Lin, W., Zhou, X., Burstein, D., et al. 2003, AJ, 126, 1286
Lintott, C. J., Schawinski, K., Keel, W., et al. 2009, MNRAS, 399, 129
Lokhorst, D., Abraham, R., van Dokkum, P., Wijers, N., & Schaye, J. 2019,
   ApJ, 877, 4
Lokhorst, D. M., Abraham, R. G., van Dokkum, P., & Chen, S. 2020, Proc.
   SPIE, 11445, 1144527
Matsubayashi, K., Sugai, H., Shimono, A., et al. 2012, ApJ, 761, 55
Mayya, Y. D., Bressan, A., Carrasco, L., & Hernandez-Martinez, L. 2006, ApJ,
   649, 172
McCourt, M., Oh, S. P., O'Leary, R., & Madigan, A.-M. 2018, MNRAS,
   473, 5407
McKeith, C. D., Castles, J., Greve, A., & Downes, D. 1993, A&A, 272, 98
McLeod, K. K., Rieke, G. H., Rieke, M. J., & Kelly, D. M. 1993, ApJ,
  412, 111
Merritt, A., van Dokkum, P., & Abraham, R. 2014, ApJL, 787, L37
Okamoto, S., Arimoto, N., Ferguson, A. M. N., et al. 2015, ApJL, 809, L1
Okamoto, S., Arimoto, N., Ferguson, A. M. N., et al. 2019, ApJ, 884, 128
Osterbrock, D. E., & Ferland, G. J. 2006, Astrophysics of Gaseous Nebulae
   and Active Galactic Nuclei (Mill Valley, CA: Univ. Science Books)
Pasha, I., Lokhorst, D., van Dokkum, P. G., et al. 2021, ApJL, 923, L21
Patterson, M. T., Walterbos, R. A. M., Kennicutt, R. C., Chiappini, C., &
   Thilker, D. A. 2012, MNRAS, 422, 401
```

```
Pettini, M., & Pagel, B. E. J. 2004, MNRAS, 348, L59
Prochaska, J. X., Hennawi, J. F., Westfall, K. B., et al. 2020, JOSS, 5, 2308
Prochaska, J. X., Hennawi, J., Cooke, R., et al. 2020, pypeit/PypeIt: Release
  1.0.0, v1.0.0, Zenodo, doi:10.5281/zenodo.3743493
Raymond, J. C. 1979, ApJS, 39, 1
Rich, J. A., Dopita, M. A., Kewley, L. J., & Rupke, D. S. N. 2010, ApJ,
  721, 505
Scannapieco, E., & Brüggen, M. 2015, ApJ, 805, 158
Schneider, E. E., Ostriker, E. C., Robertson, B. E., & Thompson, T. A. 2020,
  ApJ, 895, 43
Shopbell, P. L., & Bland-Hawthorn, J. 1998, ApJ, 493, 129
Shull, J. M., Smith, B. D., & Danforth, C. W. 2012, ApJ, 759, 23
Smercina, A., Bell, E. F., Price, P. A., et al. 2020, ApJ, 905, 60
Sofue, Y. 1998, PASJ, 50, 227
Sorgho, A., Foster, T., Carignan, C., & Chemin, L. 2019, MNRAS, 486, 504
Sparre, M., Pfrommer, C., & Vogelsberger, M. 2019, MNRAS, 482, 5401
Spitzer, L. 1998, Physical Processes in the Interstellar Medium (Weinheim:
  Wiley-VCH)
Stanghellini, L., Magrini, L., Casasola, V., & Villaver, E. 2014, A&A,
  567, A88
Thompson, T. A., Quataert, E., Zhang, D., & Weinberg, D. H. 2016, MNRAS,
  455, 1830
Tody, D. 1986, Proc. SPIE, 627, 733
Truelove, J. K., & McKee, C. F. 1999, ApJS, 120, 299
Tufte, S. L., Reynolds, R. J., & Haffner, L. M. 1998, ApJ, 504, 773
Tully, R. B., Courtois, H. M., Dolphin, A. E., et al. 2013, AJ, 146, 86
Tumlinson, J., Peeples, M. S., & Werk, J. K. 2017, ARA&A, 55, 389
van Dokkum, P. G., Abraham, R., Merritt, A., et al. 2015, ApJL, 798, L45
Watkins, A. E., Mihos, J. C., Bershady, M., & Harding, P. 2018, ApJL,
  858, L16
Westmeier, T. 2018, MNRAS, 474, 289
Yao, L. 2009, ApJ, 705, 766
Yun, M. S., Ho, P. T. P., & Lo, K. Y. 1993, ApJL, 411, L17
Yun, M. S., Ho, P. T. P., & Lo, K. Y. 1994, Natur, 372, 530
Zastrow, J., Oey, M. S., Veilleux, S., McDonald, M., & Martin, C. L. 2011,
   ApJL, 741, L17
Zhang, H., Zaritsky, D., & Behroozi, P. 2018a, ApJ, 861, 34
Zhang, J., Abraham, R., van Dokkum, P., Merritt, A., & Janssens, S. 2018b,
Zhang, J. 2021, arXiv:2109.00686
```